LETTERS
PUBLISHED ONLINE: 22 JUNE 2015 | DOI: 10.1038/NNANO.2015.131
nature nanotechnology

Graphene on hexagonal boron nitride as a tunable hyperbolic metamaterial

S. Dai[1], Q. Ma[2], M. K. Liu[1,3], T. Andersen[2], Z. Fei[1], M. D. Goldflam[1], M. Wagner[1], K. Watanabe[4], T. Taniguchi[4], M. Thiemens[5], F. Keilmann[6], G. C. A. M. Janssen[7], S-E. Zhu[7], P. Jarillo-Herrero[2], M. M. Fogler[1] and D. N. Basov[1]*

Hexagonal boron nitride (h-BN) is a natural hyperbolic material[1], in which the dielectric constants are the same in the basal plane ($\varepsilon^t \equiv \varepsilon^x = \varepsilon^y$) but have opposite signs ($\varepsilon^t\varepsilon^z < 0$) in the normal plane ($\varepsilon^z$)[1–4]. Owing to this property, finite-thickness slabs of h-BN act as multimode waveguides for the propagation of hyperbolic phonon polaritons[1,2,5]—collective modes that originate from the coupling between photons and electric dipoles[6] in phonons. However, control of these hyperbolic phonon polaritons modes has remained challenging, mostly because their electrodynamic properties are dictated by the crystal lattice of h-BN[1,2,7]. Here we show, by direct nano-infrared imaging, that these hyperbolic polaritons can be effectively modulated in a van der Waals heterostructure[8] composed of monolayer graphene on h-BN. Tunability originates from the hybridization of surface plasmon polaritons in graphene[9–13] with hyperbolic phonon polaritons in h-BN[1,2], so that the eigenmodes of the graphene/h-BN heterostructure are hyperbolic plasmon–phonon polaritons. The hyperbolic plasmon–phonon polaritons in graphene/h-BN suffer little from ohmic losses, making their propagation length 1.5–2.0 times greater than that of hyperbolic phonon polaritons in h-BN. The hyperbolic plasmon–phonon polaritons possess the combined virtues of surface plasmon polaritons in graphene and hyperbolic phonon polaritons in h-BN. Therefore, graphene/h-BN can be classified as an electromagnetic metamaterial[14] as the resulting properties of these devices are not present in its constituent elements alone.

Van der Waals (vdW) heterostructures assembled from monolayers (one or a few) of graphene, hexagonal boron nitride (h-BN), MoS_2 and other atomic crystals in various combinations are emerging as a new paradigm with which to attain desired electronic[8,15] and optical[16] properties. These heterostructures are also of interest in the context of polaritons, which are ubiquitous in metals, insulators and semiconductors[6,16]. At least two different classes of propagating polaritons are firmly established in vdW systems: surface plasmon polaritons (SP^2) in graphene[9–13] and hyperbolic phonon polaritons (HP^2) in h-BN[1,2]. In graphene/h-BN metastructures, coherent oscillations of the electron density in graphene and the atomic vibrations in h-BN produce hybridized plasmon–phonon modes. Surface plasmon–phonon modes[17] and related energy transfer processes[18] have been investigated in structures composed of graphene with monolayer h-BN or a BN nanotube. However, neither monolayers[17] nor nanotubes[18] of BN support the hyperbolic response—an exquisite attribute of three-dimensional specimens of this layered anisotropic material[1–4]. A remarkable feature of graphene/h-BN heterostructures uncovered in our experiments is that monolayer graphene impacts the hyperbolic response of h-BN slabs as thick as 99 nm (exceeding 300 atomic layers). We demonstrate that both the wavelength and intensity of hyperbolic polaritons can be controlled via electrostatic gating of the top graphene layer.

Direct experimental access to the tunable hyperbolic response in graphene/h-BN is provided by infrared nano-spectroscopy and nano-imaging via a scattering-type scanning near-field optical microscope (s-SNOM), as shown in Fig. 1a (see Methods). The same technique was used in a recent study[19] of h-BN/graphene/h-BN vdW heterostructures, but their hyperbolic spectral regions were not probed. Figure 1b presents broadband nano-infrared spectra of the normalized (see Methods) scattering amplitude $s(\omega)$ as a function of frequency $\omega = 1/\lambda_{IR}$ (λ_{IR} is the infrared wavelength) for h-BN, the SiO_2 substrate and graphene/h-BN metastructures. The spectra for SiO_2 (black) and h-BN (red) display resonances due to their mid-infrared phonons[1,20]. The two hyperbolic regions (I and II) of h-BN[1,2] are highlighted in Fig. 1b: the type I region, where $\varepsilon^z < 0$, $\varepsilon^t > 0$, extends over the frequency range $\omega = 746–819\ cm^{-1}$, and the type II region, where $\varepsilon^z > 0$, $\varepsilon^t < 0$, spans the range $\omega = 1{,}370–1{,}610\ cm^{-1}$. Both type I and II resonances of h-BN are modified in metastructures incorporating monolayer graphene (the blue spectrum in Fig. 1b). The impact of graphene is particularly prominent in the type I region, where the resonance mode is significantly enhanced and blueshifted by nearly $\sim 25\ cm^{-1}$ compared to the response of a standalone h-BN slab.

The peculiar electrodynamic response of graphene/h-BN is vividly illustrated by the calculated frequency (ω)/momentum (q) dispersion relations of its polariton modes (Fig. 1c–e; see Supplementary Section 1 for details). Following ref. 6, we visualize these dispersions using a false colour map of the imaginary part of the reflectivity r_p. It is instructive to first consider the polaritons of the two constituent elements (graphene and h-BN) separately. Figure 1c plots the dispersion of SP^2 for a freestanding graphene layer for three selected values of the Fermi energy E_F. These parabolic curves are described by the equation[21] $q_p(\omega) = ((\hbar\omega)^2/2e^2E_F)$. The corresponding plasmon wavelength is given by

$$\lambda_p = \frac{2\pi}{q_p} = \frac{4\pi e^2 E_F}{(\hbar\omega)^2} \quad (1)$$

[1]Department of Physics, University of California, San Diego, La Jolla, California 92093, USA. [2]Department of Physics, Massachusetts Institute of Technology, Cambridge, Massachusetts 02215, USA. [3]Department of Physics, Stony Brook University, Stony Brook, New York 11794-3800, USA. [4]National Institute for Materials Science, Namiki 1-1, Tsukuba, Ibaraki 305-0044, Japan. [5]Department of Chemistry and Biochemistry, University of California, San Diego, La Jolla, California 92093, USA. [6]Ludwig-Maximilians-Universität and Center for Nanoscience, 80539 München, Germany. [7]Micro and Nano Engineering Lab, Department of Precision and Microsystems Engineering, TU Delft, Mekelweg 2, 2628 CD Delft, The Netherlands. *e-mail: dbasov@physics.ucsd.edu

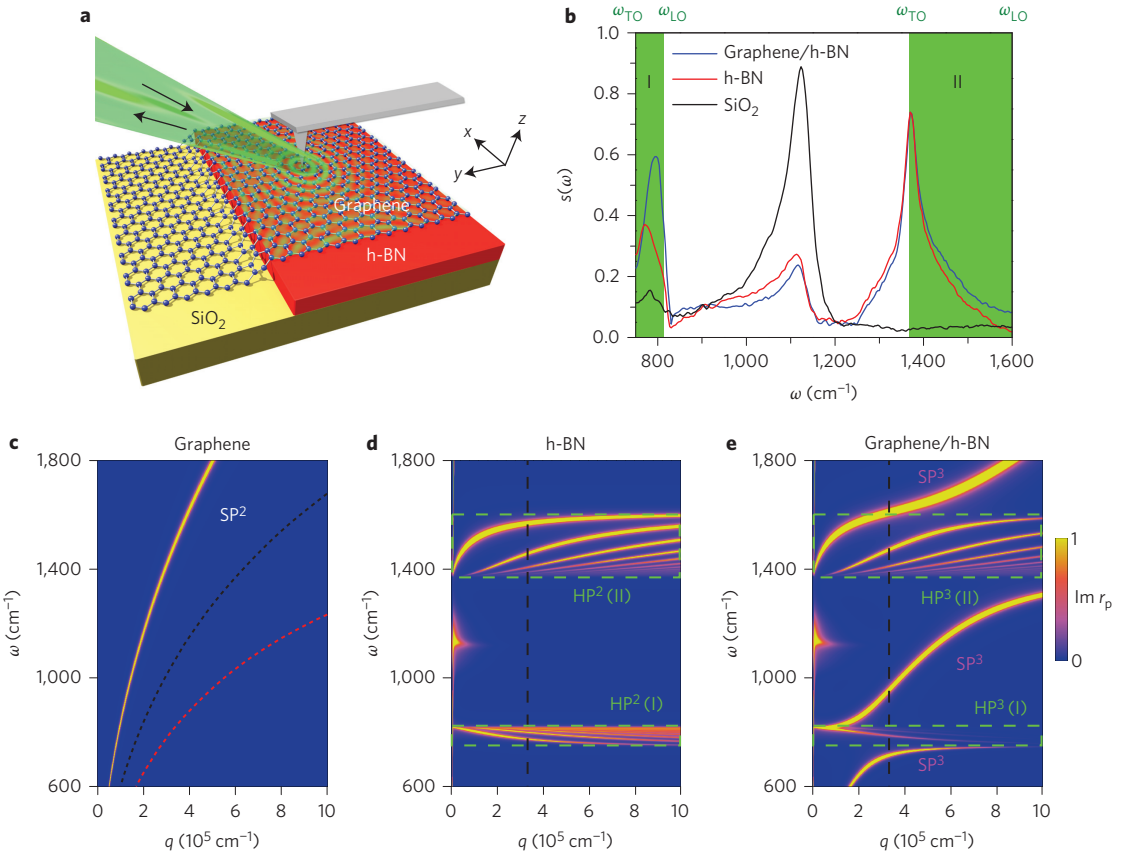

Figure 1 | Overview of the hybridized hyperbolic response in a graphene/h-BN metastructure. a, Experimental schematic showing the infrared beams (black arrows) incident on and backscattered by an atomic force microscope tip. The incident beam is generated from monochromatic or broadband laser sources (see Methods). The backscattered light is collected for extraction of the near-field signal. **b**, Broadband nano-infrared spectra of the metastructure with a representative thickness of h-BN of 58 nm. The spectra are collected far away from the sample edges where the impact of edge-reflected polaritonic waves is negligible. **c**, Calculated dispersion of the surface plasmon polaritons (SP^2) in freestanding graphene with Fermi energies of $E_F = 0.37$, 0.15 and 0.08 eV. **d**, Calculated dispersion of the hyperbolic phonon polaritons (HP^2) in h-BN of thickness 58 nm. The dispersion is visualized using a false-colour map of the imaginary part of the reflection coefficient r_p (for the case of *P*-polarization, polarized along the *z* axis, Supplementary Section 1). The black dashed line is a rough estimate of the momentum at which the tip–sample coupling is strongest[20]. Green dashed rectangles surround the regions of the hyperbolic response. **e**, As in **d**, but for a graphene/h-BN structure with $E_F = 0.37$ eV. The false-colour map reveals the dispersion of the hyperbolic plasmon–phonon polaritons (HP^3) and the surface plasmon–phonon polaritons (SP^3). Weak resonances around $\omega = 1{,}130$ cm^{-1} in **d** and **e** originate from the SiO_2 substrate.

Figure 1d plots the dispersion of HP^2 in an h-BN slab of thickness $d = 58$ nm on SiO_2 (no graphene). In a stark contrast to isotropic crystals, where longitudinal optical phonons occur at a single degenerate frequency ω_{LO}, in h-BN, multiple distinct branches of HP^2 exist[1,2,5]. These different branches correspond to quantized HP^2 waveguide modes[1,2,5] with a scalar potential oscillating across the slab and with a different number of nodes[22]. Each waveguide mode disperses between ω_{TO} and ω_{LO} (Fig. 1b). Our theoretical results and discussion in the following are relevant for all these modes. The experimental results mainly concern the principal mode, the nodeless waveguide mode of the lowest momentum. Finally, Figure 1e presents the dispersion of the new collective modes—hyperbolic plasmon–phonon polaritons (HP^3)—which arise from mixing of the SP^2 and HP^2 in the graphene/h-BN metastructure. The graphene Fermi energy $E_F = 0.37$ eV was estimated from the surface polariton wavelength in Fig. 3d (see also ref. 19). The modification of the hyperbolic response by graphene is clearly manifested in the blueshift of the HP^3 frequencies with respect to those of HP^2 (Fig. 1d,e). The shift of momenta (at a fixed frequency) is opposite in the two hyperbolic bands: negative in the type II band and positive in the type I band (Supplementary Sections 1 and 2). This contrasting behaviour stems from the fact that the polariton dispersion is negative and positive in the type I and II regions, respectively.

The change in the polariton wavelength induced by graphene is described by the equation (Supplementary Section 1)

$$\Delta\lambda(\%) = \frac{\lambda_{HP^3} - \lambda_{HP^2}}{\lambda_{HP^2}} \simeq \frac{\lambda_p}{\pi d}\frac{\varepsilon^z}{1-\varepsilon^z\varepsilon^t} \quad (2)$$

In a typical situation where ε^z, ε^t are neither too large nor too small, this formula predicts that $\Delta\lambda(\%)$ is on the order of the ratio of the two length scales: the plasmon wavelength λ_p of graphene and the thickness d of h-BN. This clarifies why the influence of graphene remains substantial in h-BN as thick as $d = 300$ nm (value obtained from calculations in Supplementary Section 1). The length scale over which graphene can exert its influence on the electrodynamics of surrounding media is set by its plasmon wavelength. Importantly, the plasmon wavelength can be controlled over a wide range by means of an applied gate voltage. Thus, HP^3 inherit the hyperbolic nature of HP^2 while gaining an important added virtue: tunability with applied gate voltage. Outside the two HP^3 regions, the plasmonic character of the dispersion is largely preserved (Fig. 1e). The

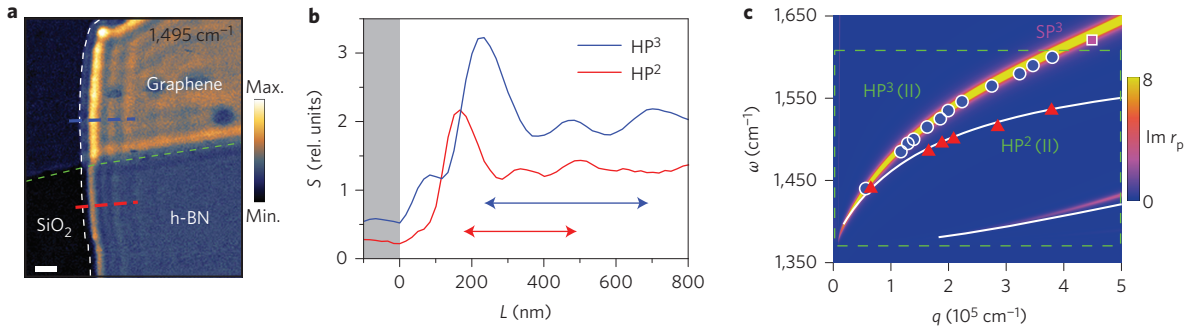

Figure 2 | Modification of type II hyperbolic phonon polaritons in a graphene/h-BN metastructure. a, Near-field amplitude image of the graphene/h-BN at frequency $\omega = 1{,}495$ cm^{-1}. With monolayer graphene, the intensity and wavelength of phonon polaritons in pristine h-BN increase. White and green dashed lines indicate the edges of the h-BN and graphene, respectively. Scale bar, 300 nm, $d = 25$ nm. **b**, Line profiles taken along the dashed blue and red lines in **a**. Double arrows indicate the polariton wavelength measured on graphene/h-BN (blue) and h-BN (red). **c**, Experimental dispersion relation of type II HP^2 in h-BN (red triangles), HP^3 (blue circles) and SP^3 in graphene/h-BN (pink square) with a Fermi energy of $E_F = 0.37$ eV. Corresponding simulation results are also provided as white lines and a false-colour map.

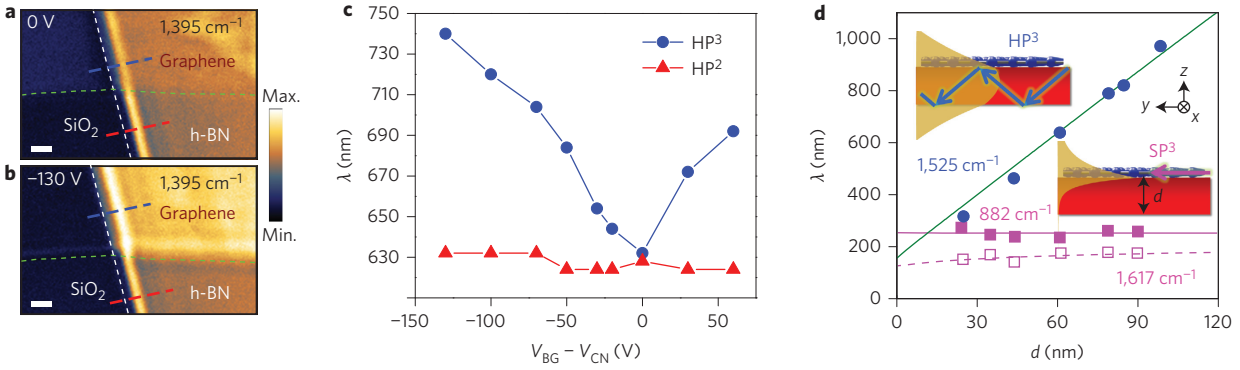

Figure 3 | Tuning of the graphene/h-BN polariton wavelength by electrostatic gating and varying the metastructure thickness. a,**b**, Near-field images of graphene/h-BN and h-BN polaritons at back-gate (BG) voltages relative to the charge neutral (CN) state $V_{BG} - V_{CN} = 0$ V (**a**) and −130 V (**b**). Scale bars, 300 nm. **c**, Gate voltage dependence of the HP^3 wavelength in a graphene/h-BN metastructure (blue dashed line in **a**,**b**) and the apparent lack thereof for HP^2 in h-BN (red dashed line in **a**,**b**) at $\omega = 1{,}395$ cm^{-1}. Thickness of the h-BN in **a**–**c**: $d = 4$ nm. **d**, Dependence of HP^3 wavelength on h-BN thickness at $\omega = 1{,}525$ cm^{-1} (data and simulations are shown as blue symbols and the green line, respectively). For the SP^3 there is no systematic thickness-dependence (filled and open pink squares at $\omega = 882$ and 1,617 cm^{-1}, respectively; corresponding simulations are plotted as solid and dashed lines). Insets: propagation schematics for HP^3 (top) and SP^3 (bottom). Yellow shapes in each inset show the real part of the polariton field as a function of z obtained using Supplementary equation (S4).

polaritonic mode flattens out in the vicinity of ω_{TO} of either of the two hyperbolic bands: a consequence of mode repulsion[23]. Similar interactions between plasmons and phonons have been studied in graphene on other substrates (for example, SiO_2, SiC, ion gel and so on) and monolayer h-BN[9–13,17,20,23,24], where the hyperbolic response is not supported. Following the terminology established there, we refer to the collective modes existing outside the h-BN hyperbolic bands as surface plasmon–phonon polaritons (SP^3)[17,19].

Infrared nano-imaging data (Figs 2 and 3) visualizing the propagating polaritons in our metastructures unambiguously support the above theoretical predictions. The basic principles of polariton imaging have been described in detail elsewhere[1,5,10,11]. In short, when illuminated by the infrared beam, the s-SNOM tip launches radially propagating polariton waves (Fig. 1a). The tip then registers the interference pattern between launched and edge-reflected polaritons, yielding oscillating fringes in the scattered near-field signal. The periodicity of the fringes is one-half of the polariton wavelength (denoted generically by λ, with suitable subscripts when needed).

Figure 2a presents nano-imaging data at a representative frequency $\omega = 1{,}495$ cm^{-1} for a metastructure that includes a slab of h-BN (thickness $d = 25$ nm) partially covered by a heavily doped monolayer graphene. We observe polariton fringes in both covered (graphene/h-BN) and uncovered (h-BN) areas. In the uncovered h-BN region (the bottom half of Fig. 2a), the fringes originate from the type II hyperbolic polaritons[1,5]. In the graphene/h-BN region (the upper part of the image in the middle of Fig. 2a) we observe fringes that are stronger and have a longer oscillation period. Prominent fringes can also be detected along the graphene edge (the dashed green line). Line profiles obtained normal to the h-BN edge (Fig. 2b) help to quantify the nearly 50% increase in both amplitude and wavelength of the fringe oscillations due to the presence of doped graphene. This prominent modification is attributed to plasmon–phonon coupling and the formation of the type II HP^3 band in our metastructure (Figs 1e and 2c).

We observe a similar enhancement of polaritonic oscillations (Fig. 2a,b) at all ω within the type II band. The blue circles in Fig. 2c display these data in the dispersion relation: ω plotted versus the polariton momentum q, which can be read off the line profiles as $q = 2\pi/\lambda$. For comparison, we also measured the HP^2 dispersion for pristine h-BN (red triangles in Fig. 2c). Both data

sets match the theoretical calculations (false colour and white lines, Supplementary Section 1) for the principle branch of hyperbolic polaritons. In addition to the principal mode, polaritons from higher-order branches are also enhanced in graphene/h-BN (Supplementary Section 3). The largest experimentally observed $\Delta\lambda(\%) = 90\%$ in this data set is reached at $\omega = 1{,}545\ \mathrm{cm}^{-1}$. In comparison, the approximate equation (2) yields 98%, using $d = 25$ nm, $\lambda_p = 180$ nm (equation (1)), $\varepsilon^z = 2.77$ and $\varepsilon^t = -1.98$. The agreement between the experiment, analytical theory and numerical simulations attests to the validity of the plasmon–phonon coupling approach to account for the modified spectrum of hyperbolic modes. We performed measurements for a variety of samples, for example, graphene on h-BN of different thicknesses, graphene obtained by exfoliation and chemical vapour deposition (CVD) techniques, all of which produced consistent results.

The tuning of polaritons in the type II HP^3 region via electrostatic gating (Methods) is presented in Fig. 3a,b at another representative frequency $\omega = 1{,}395\ \mathrm{cm}^{-1}$. When graphene is close to charge neutrality (Fig. 3a), the profile of propagating polaritons in graphene/h-BN is nearly indistinguishable from that in uncovered h-BN. Once graphene is doped by gating (Fig. 3b), both the intensity and wavelength of the polaritonic features increased significantly. This systematic study of gate-tunability is summarized in Fig. 3c (blue circles), where the wavelength consistently increases with the absolute value of gate voltage at fixed frequency $\omega = 1{,}395\ \mathrm{cm}^{-1}$.

Here we stress the distinction between the electrodynamics in HP^3 and SP^3 spectral regions (Fig. 1e). The latter are localized on the sample surface, whereas the former propagate through the entire graphene/h-BN metastructure (Fig. 3d, inset) in the form of guided waves. We verified the waveguiding character by examining the thickness-dependence of the HP^3 wavelength using multiple h-BN slabs covered by a large sheet of CVD graphene. The Fermi energy for all the graphene/h-BN samples was about the same, $E_F = 0.37$ eV. Both in the experiment (blue circles) and simulations (green line), the dependence of the HP^3 wavelength λ_{HP^3} on d is nearly linear, with a finite intercept (Fig. 3d and Supplementary Section 1), with $\Delta\lambda(\%)$ ranging from 70% ($d = 25$ nm) to 18% ($d = 99$ nm). This law readily follows from two analytical results: $\Delta\lambda(\%) \sim d^{-1}$ (equation (2)) and $\lambda_{HP^2} \sim d$ (ref. 1). In contrast, the localized SP^3 modes show essentially thickness-independent behaviour of the polariton fringes outside the hyperbolic region (for example, $\omega = 882$ and $1{,}617\ \mathrm{cm}^{-1}$). The fundamental difference between HP^3 and SP^3 is further illustrated by polariton field simulations (yellow traces in Fig. 3d, inset). The field distribution of HP^3 in graphene/h-BN is characteristic of a standing wave, whereas that of the SP^3 is localized at the graphene/h-BN interface and decays evanescently in the interior of the h-BN.

We conclude by pointing out that the tunable hyperbolic response in graphene/h-BN devices does not introduce evident losses (Fig. 2b). The loss factor of HP^3, defined as κ/q for the complex momentum $q + i\kappa$ (ref. 6), can be as small as 0.06 but increases up to ~0.10 in the vicinity of the longitudinal phonon mode. In fact, the propagation length of HP^3 in graphene/h-BN is a factor of 1.5–2.0 longer than HP^2 in h-BN (Fig. 2). The continuous and reversible *in situ* tunability of hybrid polaritons in graphene/h-BN metastructures demonstrated here (Fig. 3) is a significant advantage over other artificial and natural hyperbolic materials[1–4] and is appealing from both the perspective of fundamental physics as well as potential applications[3–5,25–29]. Thus, our work uncovers a practical approach for nanophotonic metastructures with intertwined electronic, plasmonic, phononic and/or exciton polaritonic properties[16]. Specifically, vdW polaritonic heterostructures with locally tunable properties fulfil the essential prerequisites for the implementation of transformation two-dimensional plasmonics[30,31]. The hybridization and graphene-induced tunability reported here are expected to be generic for other electromagnetic metamaterials[32] and vdW heterostructures[8,16]. A precondition for these effects is an overlap between the various polaritonic dispersion branches. Finally, we remark that it is possible to make an analogy between altering the polariton dispersion with graphene and the Goos–Hänchen effect: a lateral shift of an optical beam upon reflection from an interface[33]. The theory of such a polaritonic effect will be reported elsewhere.

Methods

Methods and any associated references are available in the online version of the paper.

Received 27 January 2015; accepted 25 May 2015; published online 22 June 2015

References

1. Dai, S. *et al.* Tunable phonon polaritons in atomically thin van der Waals crystals of boron nitride. *Science* **343,** 1125–1129 (2014).
2. Caldwell, J. D. *et al.* Sub-diffractional volume-confined polaritons in the natural hyperbolic material hexagonal boron nitride. *Nature Commun.* **5,** 5221 (2014).
3. Guo, Y., Newman, W., Cortes, C. L. & Jacob, Z. Applications of hyperbolic metamaterial substrates. *Adv. Optoelectron.* **2012,** 452502 (2012).
4. Poddubny, A., Iorsh, I., Belov, P. & Kivshar, Y. Hyperbolic metamaterials. *Nature Photon.* **7,** 948–957 (2013).
5. Dai, S. *et al.* Subdiffractional focusing and guiding of polaritonic rays in a natural hyperbolic material. *Nature Commun.* **6,** 6963 (2015).
6. Novotny, L. & Hecht, B. *Principles of Nano-Optics* (Cambridge Univ. Press, 2006).
7. Xu, X. G. *et al.* One-dimensional surface phonon polaritons in boron nitride nanotubes. *Nature Commun.* **5,** 4782 (2014).
8. Geim, A. K. & Grigorieva, I. V. Van der Waals heterostructures. *Nature* **499,** 419–425 (2013).
9. Ju, L. *et al.* Graphene plasmonics for tunable terahertz metamaterials. *Nature Nanotech.* **6,** 630–634 (2011).
10. Chen, J. *et al.* Optical nano-imaging of gate-tunable graphene plasmons. *Nature* **487,** 77–81 (2012).
11. Fei, Z. *et al.* Gate-tuning of graphene plasmons revealed by infrared nano-imaging. *Nature* **487,** 82–85 (2012).
12. Fang, Z. *et al.* Active tunable absorption enhancement with graphene nanodisk arrays. *Nano Lett.* **14,** 299–304 (2014).
13. Gerber, J. A., Berweger, S., O'Callahan, B. T. & Raschke, M. B. Phase-resolved surface plasmon interferometry of graphene. *Phys. Rev. Lett.* **113,** 055502 (2014).
14. Cai, W. & Shalaev, V. *Optical Metamaterials: Fundamentals and Applications* (Springer, 2010).
15. Fiori, G. *et al.* Electronics based on two-dimensional materials. *Nature Nanotech.* **9,** 768–779 (2014).
16. Xia, F., Wang, H., Xiao, D., Dubey, M. & Ramasubramaniam, A. Two-dimensional material nanophotonics. *Nature Photon.* **8,** 899–907 (2014).
17. Brar, V. W. *et al.* Hybrid surface-phonon–plasmon polariton modes in graphene/monolayer h-BN heterostructures. *Nano Lett.* **14,** 3876–3880 (2014).
18. Xu, X. G. *et al.* Mid-infrared polaritonic coupling between boron nitride nanotubes and graphene. *ACS Nano* **8,** 11305–11312 (2014).
19. Woessner, A. *et al.* Highly confined low-loss plasmons in graphene–boron nitride heterostructures. *Nature Mater.* **14,** 421–425 (2015).
20. Fei, Z. *et al.* Infrared nanoscopy of dirac plasmons at the graphene–SiO_2 interface. *Nano Lett.* **11,** 4701–4705 (2011).
21. Wunsch, B., Stauber, T., Sols, F. & Guinea, F. Dynamical polarization of graphene at finite doping. *New J. Phys.* **8,** 318 (2006).
22. Kumar, A., Low, T., Fung, K. H., Avouris, P. & Fang, N. X. Tunable light–matter interaction and the role of hyperbolicity in graphene–hBN system. *Nano Lett.* **15,** 3172–3180 (2015).
23. Hwang, E. H., Sensarma, R. & Das Sarma, S. Plasmon–phonon coupling in graphene. *Phys. Rev. B* **82,** 195406 (2010).
24. Yan, H. *et al.* Damping pathways of mid-infrared plasmons in graphene nanostructures. *Nature Photon.* **7,** 394–399 (2013).
25. Liu, Z., Lee, H., Xiong, Y., Sun, C. & Zhang, X. Far-field optical hyperlens magnifying sub-diffraction-limited objects. *Science* **315,** 1686 (2007).
26. Li, P. *et al.* Hyperbolic phonon–polaritons in boron nitride for near-field optical imaging. Preprint at http://arXiv.org/abs/1502.04093 (2015).
27. Hoffman, A. J. *et al.* Negative refraction in semiconductor metamaterials. *Nature Mater.* **6,** 946–950 (2007).
28. Jacob, Z., Alekseyev, L. V. & Narimanov, E. Optical hyperlens: far-field imaging beyond the diffraction limit. *Opt. Express* **14,** 8247–8256 (2006).
29. Smith, D. R., Schurig, D., Mock, J. J., Kolinko, P. & Rye, P. Partial focusing of radiation by a slab of indefinite media. *Appl. Phys. Lett.* **84,** 2244–2246 (2004).
30. Vakil, A. & Engheta, N. Transformation optics using graphene. *Science* **332,** 1291–1294 (2011).
31. Kadic, M. *et al.* Transformation plasmonics. *Nanophotonics* **1,** 51 (2012).

32. Iorsh, I. V., Mukhin, I. S., Shadrivov, I. V., Belov, P. A. & Kivshar, Y. S. Hyperbolic metamaterials based on multilayer graphene structures. *Phys. Rev. B* **87,** 075416 (2013).
33. Goos, F. & Hänchen, H. Ein neuer und fundamentaler Versuch zur Totalreflexion. *Ann. Phys.* **436,** 333–346 (1947).

Acknowledgements

Work at the University of California, San Diego (UCSD), on optical phenomena in vdW materials is supported by DOE-BES DE-FG02-00ER45799 and the Moore Foundation. Research at UCSD on metamaterials and the development of nano-infrared instrumentation is supported by the Air Force Office of Scientific Research (AFOSR), the University of California Office of The President and the Office of Naval Research. P.J-H. acknowledges support from the AFOSR (grant no. FA9550-11-1-0225).

Author contributions

S.Z. provided the CVD graphene samples used to collect data in Figs 2 and 3. All other authors were involved in designing the research, performing the research and writing the manuscript.

Additional information

Supplementary information is available in the online version of the paper. Reprints and permissions information is available online at www.nature.com/reprints. Correspondence and requests for materials should be addressed to D.N.B.

Competing financial interests

F.K. is one of the cofounders of Neaspec and Lasnix, producer of the s-SNOM and infrared source used in this work. All other authors declare no competing financial interests.

Methods

Experimental set-up. The infrared nano-imaging and Fourier transform infrared nano-spectroscopy (nano-FTIR) experiments introduced in the main text were performed using a s-SNOM, which was a commercial system (www.neaspec.com) based on a tapping-mode atomic force microscope (AFM). In the experiments, we used a commercial AFM tip (tip radius of ~10 nm) with a $PtIr_5$ coating. The AFM tip was illuminated by monochromatic quantum cascade lasers (QCLs) (www.daylightsolutions.com), CO_2 lasers (www.accesslaser.com) and a broadband laser source via difference frequency generation (DFG) (www.lasnix.com). Together, these lasers covered a frequency range of 700–2,300 cm^{-1} in the mid-infrared. The s-SNOM nano-images were recorded by a pseudo-heterodyne interferometric detection module with an AFM tapping frequency of 280 kHz and tapping amplitude around 70 nm. With this set-up, the s-SNOM was able to probe the optical signal from sub-surface objects up to a depth of ~250 nm. To subtract the background signal, the s-SNOM output signal was demodulated at the third harmonics of the tapping frequency. In this work, the near-field data are reported in the form of the normalized scattering amplitude using gold as the reference: $s(\omega) = s_{sample}(\omega)/s_{Au}(\omega)$.

Sample fabrication. h-BN crystals were mechanically exfoliated from bulk samples and deposited onto Si wafers capped with 300-nm-thick SiO_2. Graphene was then placed onto the h-BN using a polymethyl methacrylate transfer method. The graphene used in this work was obtained either via mechanical exfoliation or CVD synthesis. Similar results were obtained using both techniques. The gold film used as the reference in the measurements was lithographically fabricated on the same substrate. Electrostatic back-gating was accomplished by applying the voltage between the Si wafer and the graphene layer, with SiO_2 and h-BN as gate dielectrics.

nature nanotechnology

SUPPLEMENTARY INFORMATION

DOI: 10.1038/NNANO.2015.131

Graphene on hexagonal boron nitride as a tunable hyperbolic metamaterial

S. Dai, Q. Ma, S. -E. Zhu, M. K. Liu, T. Andersen, Z. Fei, M. D. Goldflam, M. Wagner, K. Watanabe, T. Taniguchi, M. Thiemens, F. Keilmann, G. C. A. M. Janssen, P. Jarillo-Herrero, M. M. Fogler, D. N. Basov.

DOI: 10.1038/NNANO.2015.131

1. Response functions and eigenmode dispersion of graphene-boron nitride heterostructures

In our theoretical model we treat graphene/h-BN/SiO_2 structure as an infinite stratified medium consisting of three regions: $z > 0$ (vacuum, $j = 0$), $-d < z < 0$ (h-BN, $j = 1$), and $z < -d$ (SiO_2, $j = 2$). We allow for possibility of a uniaxial anisotropy of each of the regions and denote by $\varepsilon_j^t = \varepsilon_j^t(\omega)$ and $\varepsilon_j^z = \varepsilon_j^z(\omega)$, respectively, their in-plane and the z-axis dielectric functions. (In reality, only the middle region is optically anisotropic.) The dielectric functions of h-BN are taken from Ref. S1 and those of SiO_2 from Ref. S2. Graphene layer is treated as a two-dimensional layer with sheet conductivity $\sigma(q,\omega)$ given by (Ref. S3):

$$\sigma = -i\frac{e^2}{4\hbar}\frac{\zeta}{\sqrt{v^2q^2-\zeta^2}}\left[1+G\left(\frac{\hbar\zeta+2E_F}{\hbar vq}\right)-G\left(\frac{\hbar\zeta-2E_F}{\hbar vq}\right)\right]-\frac{2i}{\pi}\frac{e^2\omega E_F}{(\hbar vq)^2}, \qquad (S1)$$
$$G(\alpha) = -\frac{1}{\pi}\left(\alpha\sqrt{1-\alpha^2}-\arccos\alpha\right), \quad \zeta = \omega+\frac{i}{\tau}.$$

Here E_F is the graphene Fermi energy, v is the Fermi velocity, and τ^{-1} is the phenomenological relaxation rate. Following the standard procedure, for the case of the *P*-polarization, the in-plane electric field in the system is written as $E_x(x,z) = e^{iqx}e_x(z)$, where the amplitude function $e_x(z)$ is the sum of two counter-propagating waves:

$$e_x(z) = A_j e^{-ik_j^z z} + B_j e^{ik_j^z z}, \quad k_j^z = \sqrt{\varepsilon_j^t\left(\frac{\omega^2}{c^2}-\frac{q^2}{\varepsilon_j^z}\right)}, \quad \Im\mathrm{m}\, k_j^z > 0. \qquad (S2)$$

The coefficients A_j and B_j can be expressed in terms of the reflection coefficients r_{ij} at the interfaces, defined by

$$r_{01} = \frac{Q_1-Q_0+S}{Q_1+Q_0+S}, \qquad r_{10} = \frac{Q_0-Q_1+S}{Q_0+Q_1+S}, \qquad r_{12} = \frac{Q_2-Q_1}{Q_2+Q_1}, \qquad (S3)$$
$$Q_j = \frac{\varepsilon_j^t}{k_j^z}, \qquad S = \frac{4\pi}{\omega}\sigma(q,\omega).$$

For a particular choice of the overall normalization factor, these expressions are

$$A_0 = -r_P^{-1}B_0, \qquad B_0 = -\frac{r_{01}+r_{12}(1-r_{01}-r_{10})e^{2ik_1^z d}}{1-r_{01}}, \qquad (S4)$$
$$A_1 = 1, \qquad B_1 = -r_{12}e^{2ik_1^z d},$$
$$A_2 = (1-r_{12})e^{i(k_1^z-k_2^z)d}, \quad B_2 = 0.$$

The total complex reflectivity r_P of the structure is given by

$$r_P = \frac{r_{01}+r_{12}(1-r_{01}-r_{10})e^{2ik_1^z d}}{1-r_{10}r_{12}e^{2ik_1^z d}}. \qquad (S5)$$

(The subscript "P" in r_P stands for the P-polarization. The remaining S-polarization is not important in the near-field limit, $q \gg \omega/c$, we study here.)

In an idealized non-dissipative system, $r_P(q,\omega)$ can have poles at real ω and q. At such poles the amplitude A_0 of the incident wave vanishes, so that the field distribution described by Eq. (S4) is self-sustained, i.e., an eigenmode. As one can see from Eq. (S5), the equation for the poles is

$$1 - r_{10} r_{12} e^{2ik_1^z d} = 0. \qquad \text{(S6)}$$

If the frequency ω belongs to a hyperbolic region, this equation has infinite number of solutions q_l corresponding to different branches of hyperbolic plasmon-phonon polaritons (HP^3). Here l is an integer that labels the branch. In the near-field limit $q \gg \omega/c$, which is realized in our experiment, we can use the approximation

$$\frac{k_j^z}{q} \simeq i\frac{\varepsilon_j(\omega)}{\varepsilon_j^z(\omega)}\ , \quad \varepsilon_j(\omega) \equiv \sqrt{\varepsilon_j^t(\omega)}\sqrt{\varepsilon_j^z(\omega)}\ , \qquad \text{(S7)}$$

to transform the equation q_l into the form similar to Eq. (1) of Ref. S4:

$$q_l(\omega) = \frac{\pi}{[-\tan\theta(\omega)]\, d}\,[l - f(q_l,\omega)]\,, \qquad \tan\theta(\omega) = i\frac{\varepsilon_1(\omega)}{\varepsilon_1^z(\omega)}\,. \qquad \text{(S8)}$$

Note that the quantity $\tan\theta$ is real. It specifies the slope of the polariton propagation direction in h-BN with respect to the z-axis. In the type II hyperbolic band where most of our experimental data are taken, we have $\tan\theta < 0$ and $f(q_l,\omega) < 0$ (see below), and so the dispersion branches with positive momentum q_l are obtained choosing $l = 0,\ 1,\ 2, \ldots$ Conversely, in the type I band $\tan\theta > 0$ and negative l should be chosen. Function $f(q,\omega)$ in Eq. (S8) represent the phase shift (normalized to 2π) of the polariton internal reflections off the h-BN surfaces. Since there two such surfaces (top and bottom), it is the sum of two terms:

$$f(q_l,\omega) = -\frac{1}{\pi}\arctan\left[\frac{i\varepsilon_0(\omega)}{\varepsilon_1(\omega)}\left(1 - \frac{2q}{q_p(\omega)}\right)\right] - \frac{1}{\pi}\arctan\left[\frac{i\varepsilon_2(\omega)}{\varepsilon_1(\omega)}\right]\ , \qquad \text{(S9)}$$

where

$$q_p(\omega) \equiv \frac{i\omega\varepsilon_0}{2\pi\sigma\left(q_p,\omega\right)} \simeq \frac{\varepsilon_0}{e^2}\,\frac{(\hbar\omega)^2}{2E_F} \qquad \text{(S10)}$$

has the physical meaning of the plasmon momentum in free-standing graphene. (More precisely, it is the plasmon momentum of graphene in a medium with dielectric constant ε_0. Note also that the second equality in Eq. (S10) is the same as Eq. (1) of the main text except therein we replaced ε_0 by unity, to lighten the notations.)

Upon examination of Eqs. (S8) and (S9), we conclude that the HP^3 wavelength $\lambda_l = 2\pi/q_l$ must fall into the interval between λ_l^{ins} and λ_l^{met}:

DOI: 10.1038/NNANO.2015.131

$$\lambda_l^{\mathrm{ins}}(\omega) = 2d\,\frac{[-\tan\theta(\omega)]}{l - f^{\mathrm{ins}}(\omega)}\,, \qquad \lambda_l^{\mathrm{met}}(\omega) = 2d\,\frac{[-\tan\theta(\omega)]}{l - f^{\mathrm{met}}(\omega)}\,, \tag{S11}$$

where the phase shifts $f^{\mathrm{ins}}(\omega)$ and $f^{\mathrm{met}}(\omega)$ are defined by

$$f^{\mathrm{ins}}(\omega) = -\frac{1}{\pi}\arctan\left[\frac{i\varepsilon_0(\omega)}{\varepsilon_1(\omega)}\right] - \frac{1}{\pi}\arctan\left[\frac{i\varepsilon_2(\omega)}{\varepsilon_1(\omega)}\right], \tag{S12}$$

$$f^{\mathrm{met}}(\omega) = \frac{1}{2} - \frac{1}{\pi}\arctan\left[\frac{i\varepsilon_2(\omega)}{\varepsilon_1(\omega)}\right]. \tag{S13}$$

(In our system where $\varepsilon_2 > \varepsilon_0 = 1$ in the hyperbolic spectral regions both f^{ins} and f^{met} are negative.) The bound $\lambda_l^{\mathrm{met}}(\omega)$ is reached if the graphene sheet is replaced by a perfect metal with infinite conductivity. The other bound $\lambda_l^{\mathrm{ins}}(\omega)$ is obtained if the graphene sheet is treated as a perfect insulator with vanishing conductivity. Obviously, the latter is the same as the wavelength of hyperbolic phonon polaritons (HP^2) modes in an h-BN crystal without graphene[S4]. In practice, we deal with an intermediate case, and so to find q_l we need to solve the transcendental equation Eq. (S8). An approximate solution can be derived as follows. We note that most of our experimental data are taken at frequencies where $|\varepsilon_1(\omega)|$ given by Eq. (S7) is only modestly large and also λ_l is comparable or larger than the plasmon wavelength $\lambda_p \equiv 2\pi/q_p$ (which is about 190 nm at $E_F = 0.37$ eV, see Fig. 1 of the main text). In this regime it is permissible to expand function $f(q,\omega)$ in Eq. (S9) to the first order in q. After simple algebra, one can find an analytical expression for the fractional change of the polariton wavelength. Interestingly, it is l-independent and is given by

$$\frac{\lambda_l - \lambda_l^{\mathrm{ins}}}{\lambda_l^{\mathrm{ins}}} \simeq \frac{\lambda_p}{\pi d}\,\frac{\varepsilon_0\varepsilon_1^z}{\varepsilon_0^2 - \varepsilon_1^z\varepsilon_1^t}\,, \quad \frac{\lambda_l}{\lambda_p} \gg \min\left\{\frac{\varepsilon_0}{|\varepsilon_1(\omega)|}, 2\right\}. \tag{S14}$$

(This is the same as Eq. 2 of the main text except therein we replaced ε_0 by unity and dropped the subscripts of ε_1^z, ε_1^t, to lighten the notations once again.) Equation (S14) accounts for the key experimental observations. First, it shows that at a fixed frequency, addition of graphene decreases the polariton wavelength in the type I spectral band and increases it in the type II one. This agrees with the experimental results presented in Fig. 2 of the main text and Fig. S2d below and also with the numerical results shown in Figs. 2c, S1, and S2c. Next, Eq. (S14) clarifies which material parameters determine the magnitude of the observed wavelength variation. As expected, the fractional change in the wavelength decreases with h-BN thickness d. The range of d where it remains appreciable is proportional to the plasmon wavelength λ_p of graphene in vacuum and is approximately inversely proportional to the in-plane dielectric function of h-BN $\varepsilon_1^t(\omega)$. This explains why the influence of monolayer graphene on polaritons in rather thick h-BN crystals is still readily observable. For example, at $\omega = 1525\ \mathrm{cm}^{-1}$

where $\varepsilon_1^t = -2.9$, $\varepsilon_1^z = 2.8$, Eq. (14) predicts a $\Delta\lambda(\%) = 80\%$ wavelength change for $d = 25$ nm (Fig. 2c) and a $\Delta\lambda(\%) = 20\%$ change at $d = 100$ nm (Fig. 3d).

If the thickness is fixed, the fractional change in λ_l grows as ω approaches the top of the type II band, where $\varepsilon_1(\omega)$ tends to zero. This is again in agreement with the numerical results in Fig. S1. Note that in this frequency range one eventually enters the regime $|\varepsilon_1(\omega)| \ll \varepsilon_0$ in which the domain of validity of Eq. (S14) is restricted to $\lambda_l > 2\lambda_p$. At $\lambda_l < 2\lambda_p$ (or equivalently, at $q > q_p/2$) the polariton wavelength λ_l should approach the perfect-metal bound $\lambda_l^{\mathrm{met}}(\omega)$ [Eq. (S11)]. The crossover to this limiting value is sharp, almost step-like if$|\varepsilon_1(\omega)| \ll \varepsilon_0$. If $|\varepsilon_1(\omega)| \sim \varepsilon_0$, this crossover is smooth.

For the absolute change of the wavelength, Eqs. (S8), (S11), and (S14) yield

$$\lambda_l \simeq \lambda_l^{\mathrm{ins}} - \frac{2}{\pi}\frac{i\varepsilon_0\varepsilon_1}{\varepsilon_0^2 - \varepsilon_1^z\varepsilon_1^t}\frac{\lambda_p}{l - f^{\mathrm{ins}}}\,, \qquad \frac{\lambda_l}{\lambda_p} \gg \min\left\{\frac{\varepsilon_0}{|\varepsilon_1(\omega)|}, 2\right\}. \tag{S15}$$

This formula is consistent with the observed linear thickness dependence of the HP[3] wavelength at constant frequency (Fig. 3d of the main text). Indeed, the first term on the right-hand side of Eq. (S15) is linear in d, while the second term is thickness-independent. If $l \neq 0$, at very small d the inequality indicated in Eq. (S15) can be violated, in which case the dependence on d should become sublinear and eventually flatten out. For the principal branch $l = 0$, a particularly formula for the polariton wavelength can be obtained for frequencies $\omega \simeq \omega_{\mathrm{TO}}$ near the bottom of the hyperbolic bands. Using Eqs. (S12) and (S15), we find

$$\lambda_0 \simeq \frac{2}{\varepsilon_0 + \varepsilon_2}\left(\pi\varepsilon_1^t d + \varepsilon_0\lambda_p\right), \qquad |\varepsilon_1(\omega)| \gg \varepsilon_0, \varepsilon_2\,. \tag{S16}$$

This equation predicts the linear in thickness behavior of λ_0 down to $d = 0$. Note that ε_1^z does not enter Eq. (S16); hence, the anisotropy of h-BN does not play much role in this regime. Our experimental data for gated G-h-BN structures shown by the blue circles in Fig. 3c of the main text are in a qualitative agreement with Eq. (S16).

The foregoing discussion neglected dissipation always present in real materials. Because of such dissipation $r_P(q,\omega)$ never diverges at any real ω and q. As long as the dissipation is weak, we can still define eigenmodes dispersions; however, it is convenient to get them not from the poles of $r_P(q,\omega)$ but from the locations of resonances (sharp maxima) of function $\Im\mathrm{m}\, r_P(q,\omega)$ at real ω. This function, which in fact is the measure of dissipation, is shown as a false color map in Figs. 1d,e and 2c of the main text and Figs. S1, S2c below. The bright lines delineate the dispersions of the modes and their widths represent the frequency linewidth of the resonances. The maps in Figs. S1a-d were computed for h-BN thickness of 50, 100, 150, and 300 nm, respectively. For comparison, the dispersion of HP[2]s of a bare h-BN substrate are shown by the white lines. In agreement with Eq. (S14), the momenta of HP[3]s in

DOI: 10.1038/NNANO.2015.131

graphene/h-BN meta-structures are shifted to smaller momenta (larger wavelengths) compared to HP^{2}s. The effect remains strong for h-BN as thick as 300 nm (in general, as long as d is not much larger than λ_p). Outside the Type II hyperbolic region, surface plasmon-phonon polaritons (SP^{3}s) exhibit little dependence on the meta-structure thickness, as discussed in the main text.

To calculate the electric field profile of the eigenmodes in the presence of damping (insets of Fig. 3d of the main text), we used Eqs. (S2) and (S4) except we set coefficient A_0 to zero and set B_0 to $1 - r_{12}e^{2ik_1^z d}$, for continuity.

2. Tunable polaritons and plasmon-phonon coupling around the Type I region

Tunable hyperbolic response and plasmon-phonon coupling is also observed in the Type I hyperbolic region. Single-wavelength nano-imaging experiments in the Type I region are severely restricted by the current availability of monochromatic IR lasers necessitating the need for using broadband mid-IR laser for the following measurements. Spectroscopic data ($\omega = 600$ to 1000 cm^{-1}) were obtained with our nanoscale Fourier transform infrared spectroscopy (nano-FTIR) setup and provide a complete experimental picture of the polaritonic response in this region (Fig. S2b). It is instructive to represent these broadband data in the form of a single spectroscopic line scan (Figs. S2a-b) following Ref. S4. The line scan is plotted as a false color map of the scattering amplitude $s(\omega, L)$ which varies with infrared (IR) frequency (ω) and position (L) along the scanning direction. For bare h-BN ($L < 0$), the out-of-plane phonon generates strong signal near $\omega \sim 770$ cm^{-1}. We can examine experimental results obtained as the tip scans across the graphene edge ($L = 0$) and continues into the interior of the graphene/h-BN ($L > 0$). The h-BN phonon resonance is strongly enhanced and blue shifted as a result of the presence of monolayer graphene for $L > 0$, consistent with the spectra displayed in Fig. 1b. These findings point to tunable polaritons similar to that in the Type II region (Figs. 2-3 of the main text).

We stress that the phase and group velocity corresponding to the dispersion in the Type I region are antiparallel. This negative dispersion underlies subtle but important differences related to graphene-induced modification of phonon polaritons of h-BN. Specifically, the hybrid HP^3 modes in the Type I region reveal an increased q or reduced wavelength λ in contrast with the opposite changes observed in the Type II region (Fig. 2).

Furthermore, we wish to point out that the hybrid polariton in Type I hyperbolic region splits the surface plasmon polariton (SP^2) (Fig. 1c) of free standing graphene into two SP^{3}s ($\omega < 746$ cm^{-1} and $\omega > 819$ cm^{-1}, Fig. S2b) in graphene/h-BN. The SP^3 fringes were observed close to the graphene edge (Fig. S2b, $L > 0$). As discussed in the

main text, these SP^3s are localized to the graphene so their dispersion has effectively no dependence on the h-BN thickness (Fig. 2d). At lower frequencies (ω = 600 to 1000 cm^{-1}), both the HP^3 resonance (Fig. S2b) and SP^3s (Fig. S2b) can be tuned via electrostatic back-gating. The HP^3 resonance (bright ribbon in Fig. S2b) peaks at 780 cm^{-1} (Fig. 2d) when graphene is close to charge neutrality. As the back-gate voltage ($V_{BG} - V_{CN}$) increases (in either polarity), the HP^3 resonance is blueshifted and until reaching the boundary of Type I region (~ 815 cm^{-1}), yet another effect originating from strong plasmon-phonon coupling. Propagation of the SP^3 can be imaged with the nano-imaging technique introduced in the main text. A representative IR image (ω = 882 cm^{-1}) of a tapered graphene/h-BN is shown as the inset of Fig. S2e. The SP^3 fringes run parallel to the graphene edges. The fringes closest to the edges (white dashed lines) are the strongest and are followed by weaker, increasingly damped fringes. Similar to graphene on other substrates[S5-S9], the wavelength of SP^3 in graphene/h-BN can be tuned by varying the back-gate voltage (Fig. S2e).

3. Higher order hyperbolic polaritons in graphene/h-BN meta-structures

In this work, we provide theoretical analysis for graphene/h-BN polaritons from all hyperbolic branches. Yet the majority of experimental results are confined to the principal $l = 0$ branch for the following reason. Higher order (l = 1, 2, 3 …) polaritons are weaker and occur at much larger momenta. The increased momentum results in significantly smaller wavelengths λ as compared to the principal branch. Therefore, these polaritons are highly confined and can only be observed in its immediate vicinity of the sample edge, leading to a small oscillation (Fig. S3b, $0 < L < 150$ nm, overlapped with the green background). In spite of this, hybridization for $l \neq 0$ polaritons was also observed in our experiments, where the small oscillation was enhanced by graphene (Figs. S3a-b). However, due to the resolution limit of our nano-IR apparatus and the unknown (possibly, complicated) structure of graphene-covered h-BN edges, quantitative results for $l \neq 0$ polaritons may need future experiments.

References

S1. Cai, Y., Zhang, L., Zeng, Q., Cheng, L. & Xu, Y., Infrared reflectance spectrum of BN calculated from first principles. *Solid State Commun.* **141**, 262 (2007).

S2. Fei, Z. et al. Infrared Nanoscopy of Dirac Plasmons at the Graphene–SiO2 Interface. *Nano Lett.* **11**, 4701-4705 (2011).

DOI: 10.1038/NNANO.2015.131

S3. Wunsch, B., Stauber, T., Sols, F. & Guinea, F. Dynamical polarization of graphene at finite doping. *New J. Phys.* **8**, 318 (2006).

S4. Dai, S. et al. Tunable phonon polaritons in atomically thin van der waals crystal of boron nitride. *Science* **343**, 1125-1129 (2014).

S5. Chen, J. et al. Optical nano-imaging of gate-tunable graphene plasmons. *Nature* **487,** 77-81 (2012).

S6. Fei, Z. et al. Gate-tuning of graphene plasmons revealed by infrared nano-imaging. *Nature* **487,** 82-85 (2012).

S7. Yan, H. et al. Damping pathways of mid-infrared plasmons in graphene nanostructures. *Nature Photon.* **7**, 394-399 (2013).

S8. Gerber, J. A., Berweger, S., O'Callahan, B. T. & Raschke, M. B. Phase-Resolved Surface Plasmon Interferometry of Graphene. *Phys. Rev. Lett.* **113,** 055502 (2014).

S9. Fang, Z. et al. Active Tunable Absorption Enhancement with Graphene Nanodisk Arrays. *Nano Lett.* **14**, 299-304 (2014).

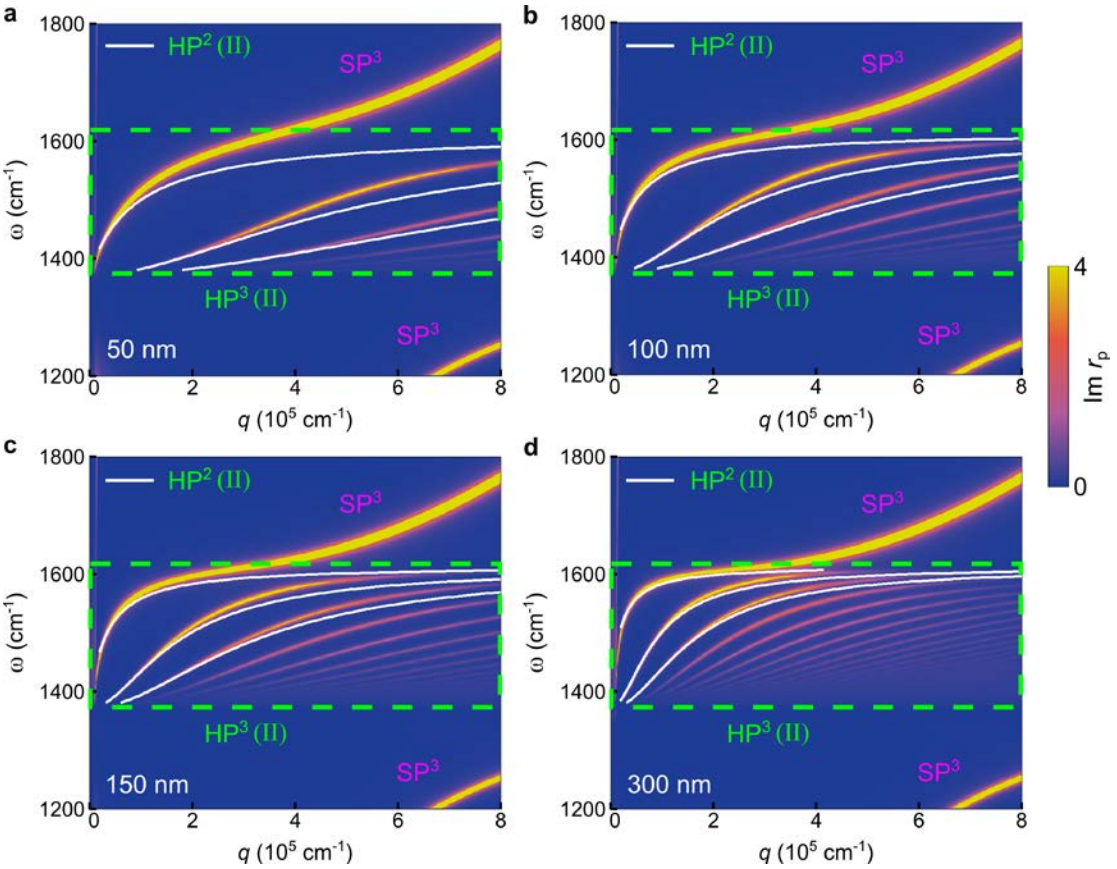

Figure S1 | Frequency (ω) - momentum (*q*) dispersion of polaritons in graphene/h-BN meta-structure with different thicknesses. a, Dispersion of hyperbolic phonon polaritons (HP^2s) in h-BN (white lines), hyperbolic plasmon-phonon polaritons (HP^3s) and surface plasmon-phonon polaritons (SP^3s) in graphene/h-BN (false color). The green dashed line marks the spectral boundaries of the type II hyperbolic region. h-BN thickness is 50 nm, the graphene Fermi energy E_F = 0.37 eV. **b–d**, Same as (**a**) for h-BN thickness 100, 150 and 300 nm, respectively.

DOI: 10.1038/NNANO.2015.131

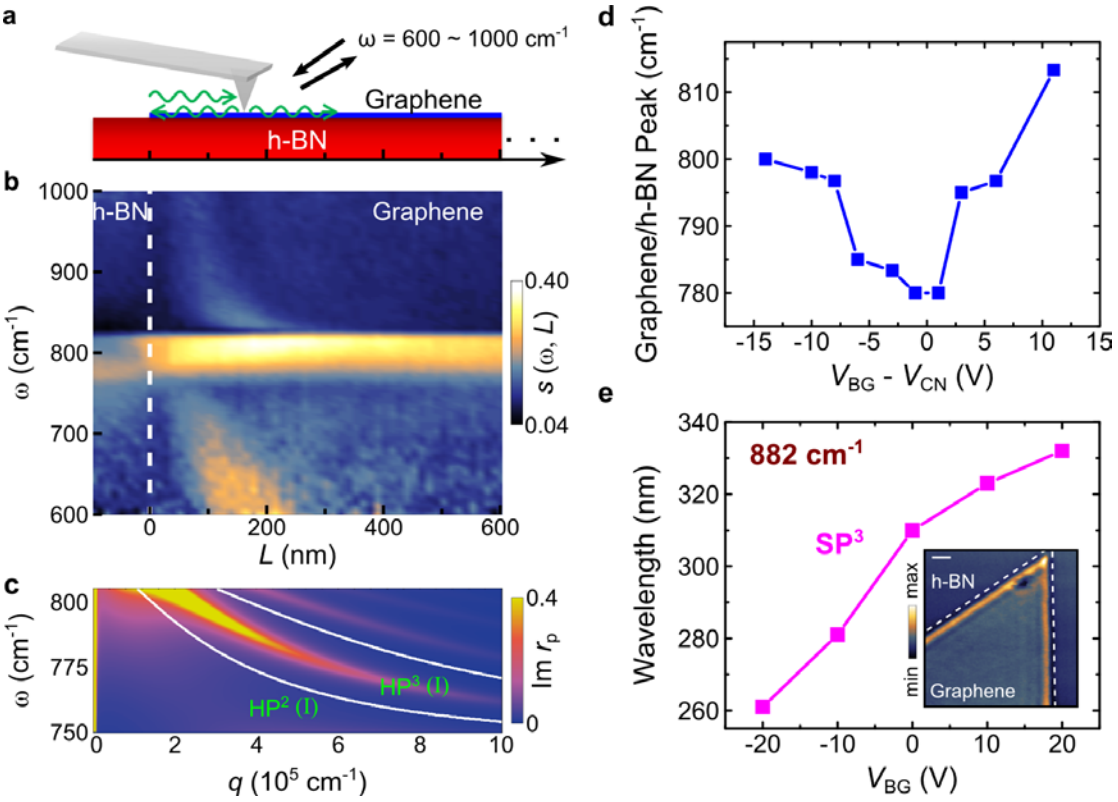

Figure S2 | Tunable hyperbolic response and hybrid polaritons in the lower frequency region (ω = 600 – 1000 cm^{-1}). **a**, Schematic of the nano-FTIR line scan experiment. Black arrows indicate incident and back-scattered IR beam. Green arrows describe the SP^{3}s launched from the AFM tip and reflected by graphene edge at $L = 0$. **b**, The polaritonic overview from 600 to 1000 cm^{-1} mapped by the nano-FTIR line scan. The scattering amplitude $s(L, \omega)$ is mapped with the false color. White dashed line marks the $L = 0$ graphene edge. **c**, The polariton dispersion in the Type I region. The HP^2 and HP^3 are plotted as white lines and false color map. Thickness of h-BN: 50nm, the graphene Fermi energy $E_F = 0.37$ eV. **d,** The HP^3 resonance peak position (bright region in Fig. S3b) as a function of the back-gate voltage V_{BG} referenced to the graphene charge-neutrality voltage V_{CN}. **e,** Back-gate voltage dependence of the SP^3 wavelength extracted from the near-field images measured at $\omega = 882$ cm^{-1} using a monochromatic laser source. Inset: a representative near-field image of the SP^3. Scale bar: 200 nm.

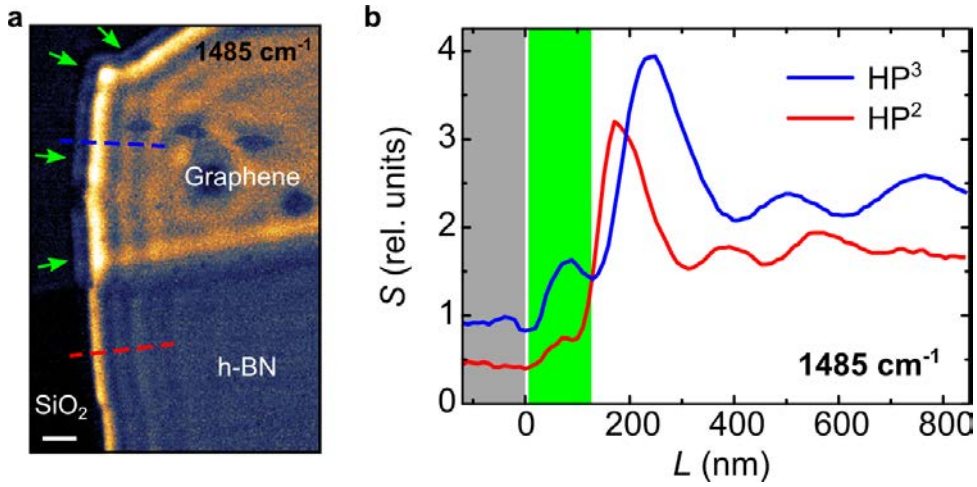

Figure S3 | Supplementary s-SNOM data for hybridization of $l \neq 0$ hyperbolic polaritons. **a**, Near-field amplitude image of the graphene/h-BN at frequency ω = 1485 cm^{-1}. A bright line (higher near-field signal, indicated by the blue arrows) formed very close to the sample edge for the part covered by graphene. Scale bar: 300 nm, d = 25 nm. **b**, Line profiles taken along the dashed lines in (**a**). The part with green background shows enhanced polaritonic features from $l \neq 0$ branches in graphene/h-BN (blue) compared with that in h-BN (red).